Ultrasonics - Sonochemistry 44 (2018) 331–339

Contents lists available at ScienceDirect

Ultrasonics - Sonochemistry

journal homepage: www.elsevier.com/locate/ultson

Ultrasonic cavitation erosion-corrosion behavior of friction stir processed stainless steel

Karthikeyan Selvam[a], Priya Mandal[b], Harpreet Singh Grewal[a], Harpreet Singh Arora[a,*]

[a] Surface Science and Tribology Lab, Department of Mechanical Engineering, Shiv Nadar University, Uttar Pradesh 201314, India
[b] Department of Physics, Shiv Nadar University, Uttar Pradesh, India

ARTICLE INFO

Keywords:
Friction stir processing
Phase transformation
Cavitation
Corrosion

ABSTRACT

Cavitation erosion remains the primary cause of material degradation in fluid machinery components operating at high speed. Micro-jets/shock waves caused by implosion of bubbles on material surface results in significant material loss and premature failure of the components. The presence of corrosive medium further exuberates this effect, causing rapid degradation. Here, we demonstrate a novel pathway to control cavitation erosion-corrosion by tailoring the surface properties using submerged friction stir processing (FSP), a severe plastic deformation process. FSP parameters were varied over wide range of strain-rates to generate tailored microstructures. High strain-rate processing resulted in nearly single phase fine grained structure while low strain-rate processing resulted in phase transformation in addition to grain refinement. As-received and processed samples were subjected to ultrasonic cavitation in distilled water as well as in corrosive environment of 3.5% NaCl solution. Individual roles of cavitation erosion, corrosion and their synergistic effects were analyzed. Depending on the microstructure, processed samples showed nearly 4–6 times higher cavitation erosion resistance compared to as-received alloy. Superior cavitation erosion-corrosion resistance of processed samples was attributed to surface strengthening, higher strain-hardening ability and quick passivation kinetics. The results of current study could be potentially transformative in designing robust materials for hydro-dynamic applications.

1. Introduction

Cavitation erosion-corrosion is one of the key reasons of material removal in high speed hydraulic machines and equipments. Compared to other material degradation processes such as slurry erosion, corrosion and wear, cavitation erosion-corrosion possess more aggravating character [1]. This is attributed to repeated implosion of vapor bubbles at supersonic speeds causing cyclic straining of the material and resulting in significant material loss [2–4]. Further, corrosive environment exacerbates material degradation under cavitation, due to constant removal of passive layer and synergetic effects of erosion and corrosion [5–7]. Development of superior metallic alloys such as austenite stainless steels with high strength, plasticity and quick passivation reduces the severity of cavitation erosion. Despite its superior mechanical properties and electrochemical resistance, austenite steels are prone to cavitation erosion owing to the complex component design and extreme operating conditions observed in hydraulic machines [8–10]. Finding a long lasting, reliable and economical solution for limiting cavitation erosion is an active area of research.

Being a surface phenomenon, tailoring the surface properties is a plausible solution to address cavitation erosion-corrosion [11–13]. Typically, surface coatings are used for limiting the material loss by degradation processes. Physical vapor deposition, chemical vapor deposition and thermal spraying remains the most widely used techniques for development of surface coatings [14–17]. Owing to its versatile nature and capability to coat nearly any composition, thermal spraying is considered as most reliable, robust and economical coating technique [18–21]. However, presence of splat boundaries, pores, un-melted particles and inherent lamellar microstructure of thermal sprayed coatings results in anisotropic behavior, poor mechanical and tribological properties. This limits the wide applicability of thermal spray coatings due to its premature failure. In contrast, tailoring surface properties of the parent material itself without changing surface chemistry is an innovative approach to circumvent the aforementioned limitations.

Severe plastic deformation (SPD) processes are widely recognized for tailoring the properties of materials through microstructural refinement [22,23]. Friction stir processing (FSP) is one such SPD process widely used for both surface and bulk modification of materials [24–26]. Previous studies report on the utilization of FSP to obtain

* Corresponding author.
E-mail address: harpreet.arora@snu.edu.in (H.S. Arora).

https://doi.org/10.1016/j.ultsonch.2018.02.041
Received 14 December 2017; Received in revised form 9 February 2018; Accepted 24 February 2018
Available online 26 February 2018

tailored microstructures varying from nano-grained to metal matrix composites [25,27,28]. However, most of these studies are limited to light metals and their alloys. FSP of high strength materials, such as stainless steel, has not been investigated in depth and lacks detailed understanding on microstructural evolution. In addition, there are very few studies on cavitation erosion behavior of friction stir processed stainless steel [29–32]. Further, the effect of phase transformation on cavitation erosion-corrosion behavior has not been evaluated.

In the current study, we used an innovative submerged friction stir processing technique to tailor the surface properties of austenitic stainless steel. Processing at different strain rates resulted in varied microstructures in stainless steel. Cavitation erosion-corrosion behavior of as-received and processed samples was investigated and individual roles of erosion, corrosion and their synergistic effects were analyzed.

2. Experimental details

2.1. Material processing

For our current investigation, austenitic steel SS316L was used. Plates with dimensions 70 mm × 50 mm × 5 mm were cut from commercially available SS316L steel. Universal milling machine, model XW6032A was utilized for performing FSP using a pin-less tungsten carbide tool to tailor only the surface characteristics of the alloy. Processing was done under submerged cooling condition with specimen completely submerged in a pool of low temperature coolant at 0 °C, circulated through an external chiller unit (Escy, model IC201-K4). The mixture of distilled water and ethanol, in equal proportion, was used as a coolant. FSP was done under two different processing conditions: at rotational speed of 388 rpm (henceforth designated as 388-C) and 1800 rpm (henceforth designated as 1800-C) with a constant traverse speed of 20 mm/min. Temperature during FSP was measured with K-type thermocouple, at a distance of 1 mm from the tool. Fig. 1 shows a schematic representation of the FSP experimental set up and the processing scheme. The processed samples were sectioned along the cross-section using low speed diamond saw (Chennai metco, model LSS003). The surface as well as cross-section samples were polished down to 3000 grit followed by fine polishing using 0.5 µm diamond paste. All samples were then electro-polished in 10% oxalic acid solution at 6 V

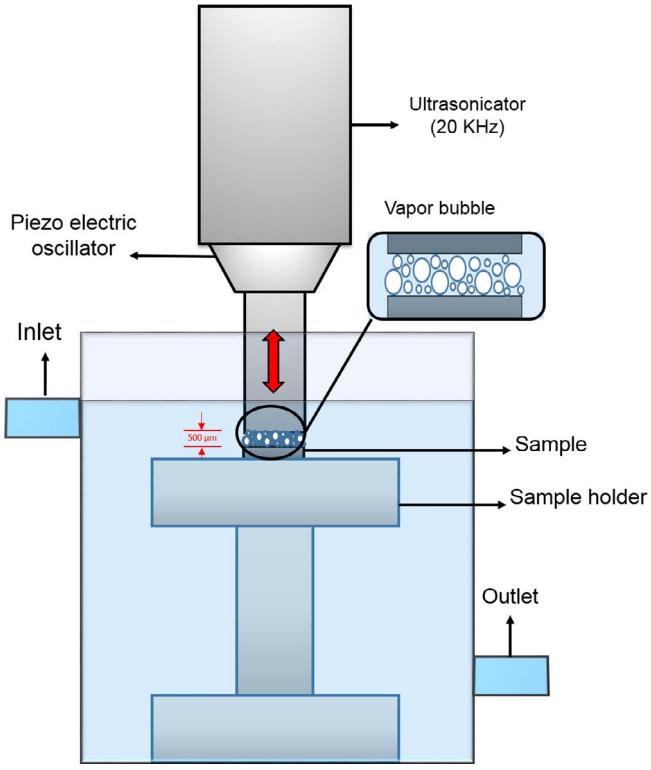

Fig. 2. Schematic representation of cavitation erosion set-up with ultrasonicator and sample holder.

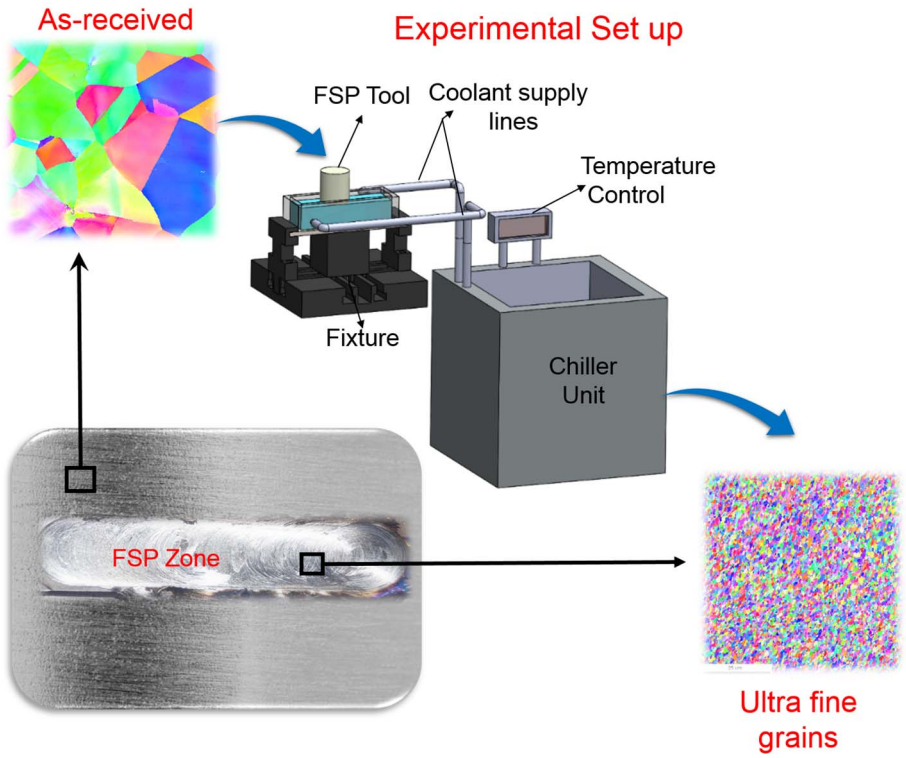

Fig. 1. Schematic representation of the submerged friction stir processing used in the current study. The as-received stainless steel has coarse grain structure while processing resulted in significant grain refinement.

for 2 min. The grain size distribution and phase transformation for the as-received and processed samples were obtained using electron back scatter diffraction (EBSD). EBSD analysis was conducted using FEI Quanta 3D FEG using step size of 0.1 μm. Hardness of the as-received and processed samples was obtained using Econonet micro-hardness tester, model VH-1MDX, while elastic modulus and strain-hardening exponent were obtained using nano-indentation (Hyistron TI 950).

2.2. Ultrasonic cavitation studies

As-received and processed samples were tested for cavitation erosion and cavitation erosion-corrosion. Tests were conducted using an ultrasonic vibratory oscillator (Make: Sonics; VCX750) at 20 ± 0.5 kHz frequency with peak to peak amplitude of 50 μm ± 5%, as per G32 ASTM standard and power intensity of 2.31 W/cm^2. The sample was placed at a stand-off distance of 500 μm below the tip. Fig. 2 shows the schematic representation of the vibratory apparatus used in the current study. For pure erosion studies, samples were submerged in a 1 L beaker containing 500 ml of distilled water whereas for erosion-corrosion studies, 500 ml of 3.5% NaCl solution was used as a medium. Temperature of the medium during testing was kept constant at 24 ± 2 °C using a cooling coil connected to the chiller. Prior to the test, all samples were grounded and polished down to 2000 grit using abrasive papers. Each sample was tested for 20 h with subsequent mass change (0.01 mg) measurements after every one-hour cycle. To ensure repeatability, two samples were tested under each condition. The surface of all eroded samples was examined using scanning electron microscope (SEM) (JEOL 6610LV) to understand the cavitation erosion mechanisms.

2.3. Corrosion testing

Static corrosion experiments were done in electrochemical cell (make: Gamry, model: 1000E) using a standard three electrode cell configuration with high density graphite rod as counter electrode, saturated calomel electrode (*SCE*) as reference and sample as working electrode. Cyclic polarization tests were done in the voltage range of −0.4 V to 1.5 V vs open circuit potential (E_{OCP}) with the forward and reverse scan rate of 0.166 mV/s.

3. Results and discussion

3.1. Microstructure and mechanical characterization

EBSD images showing the grain structure and grain size distribution for the as-received steel and both the processed specimen are shown in Fig. 3. The as-received alloy has significant fraction of grains in the range of 15–40 μm with an average grain size of nearly 22 μm (Fig. 3(b)). In contrast, both 388-C (Fig. 3(c)) and 1800-C (Fig. 3(e)) showed ultra-fine grain structure with an average grain size of nearly 0.9 μm and 0.6 μm for 1800-C and 388-C respectively. Microstructural refinement during FSP is attributed to dynamic recrystallization wherein the coarse grains are replaced by fine grained microstructure. Low stacking fault energy materials such as austenitic steel recrystallizes typically by discontinuous dynamic recrystallization (DDRX). The criteria for DDRX to occur is given by relation $\rho_m^3/\dot{\varepsilon} > 2\gamma_b/KMLGb^5$ [33] where ρ_m is the mobile dislocation density, $\dot{\varepsilon}$ is the strain rate, γ_b is the grain boundary energy, K is a constant fraction of the dislocation line energy that is stored in the newly formed grains, L is mean slip distance of dislocations in these grains, M is the boundary mobility, G is the shear modulus and b is the burger's vector. The inequality indicates that higher dislocation density favours DDRX which typically occur by distinct grain-nucleation and grain-growth phases. Prior grain boundaries act as embryonic sites for the nucleation of new grains during DDRX. As the recrystallization process proceeds, the nucleated grains form a thickening band in a necklace-like arrangement which eventually develops into fully recrystallized structure [33].

Ultra-fine grain structure for 1800-C and 388-C is attributed to deformation induced DDRX. Further, 388-C has finer grain structure compared to 1800-C while the latter has more log-normal grain size distribution (Fig. 3(d) and (f)). The nucleation frequency tends to increase at higher strain-rate due to higher stored energy [33]. Thus, the nucleation density for 1800-C is likely to be higher being deformed at significantly larger strain-rate, which explains its better log-normal grain distribution. However, higher strain-rate deformation at 1800 rpm resulted in higher peak temperature of 355 K compared to 313 K at 388 rpm, resulting in nominal grain growth for the later leading to finer grain structure. X-ray diffraction analysis for as-received and both processed samples is shown in Fig. 4(a). As-received alloy and 1800-C specimen show only austenite phase while 388-C shows both austenite and martensite phases. The EBSD phase map, shown in Fig. 4(b)–(d), also show only austenite phase for the as-received alloy. However, EBSD phase map for 1800-C shows a small fraction of martensite phase (~8%) while 388C has significantly higher martensite fraction (~45%). Austenite to martensite transformation likely occurred due to severe plastic deformation during FSP. Martensite formation during plastic deformation in stainless steels has been reported previously as well. Further, this transformation is favoured more at lower strain-rate deformation while higher strain-rate suppresses the transformation due to nearly adiabatic heating [35,36]. This explains significantly higher martensite fraction for 388-C specimen.

Micro-hardness was measured for all the samples at the surface as well as along the cross-section and is shown in Fig. 5(a). Maximum hardness for the processed samples was measured at top surface and the value decreases as a function of depth. Compared to the as-received alloy, 388-C show nearly two times and 1800-C shows nearly 1.6 times higher hardness. Increase in hardness of these samples is attributed to combined influence of grain boundary strengthening and martensite formation. Micro-hardness for 388-C and 1800-C was found to be in the range of 420 ± 10 HV to 350 ± 5 HV, respectively. Fig. 5(b) shows load-displacement curves for all the specimens obtained using nano-indentation. The elastic modulus values are given alongside. The strain-hardening exponent (n) was calculated for all samples from nano-indentation using the methodology proposed by Giannakopoulos and Suresh [37] given by the expression: $n \sim \ln\{\sigma_{0.29} - \ln(\sigma_y)\}/5$, where σ_y is yield strength of the material, $\sigma_{0.29}$ is stress corresponding to plastic strain of 0.29; $\sigma_{0.29}$ and σ_y were evaluated from the equation

$$\frac{\sigma_{0.29} - \sigma_y}{0.29E^*} = 1 - 0.142\frac{h_r}{h_{max}} - 0.957\left(\frac{h_r}{h_{max}}\right)^2$$

Table 1 shows the strain-hardening exponent for as-received alloy, 1800-C and 388-C. It is to be noted that n values obtained from nano-indentation are an approximation and may differ from those obtained by the tension test. However, since all samples are tested under similar condition so n values for different samples conveniently represent the general trend. It is seen that n is the highest for 388-C, followed by 1800-C and least for the as-received alloy indicating highest tendency of 388-C specimen to get strain-hardened. Strain-hardening ability is known to decrease with refinement in the grain size due to inability of finer grains to hold dislocations. However, in the current study, processed samples with finer grain structure showed higher strain hardening. This may be attributed to the presence of martensite phase which is known to enhance the strain hardening of the material [38]. In addition, the total indentation work (W_t), the irreversible indentation work (W_i) and the reversible indentation work (W_e) were calculated for all the samples from their respective load-displacement curves and is shown in Table 1. It is seen that both the processed samples showed higher reversible work (W_e), being highest for 388-C and lowest for the as-received alloy. The increase in W_e indicates increased elastic energy storing capacity which is associated with enhanced impact load absorbing capacity.

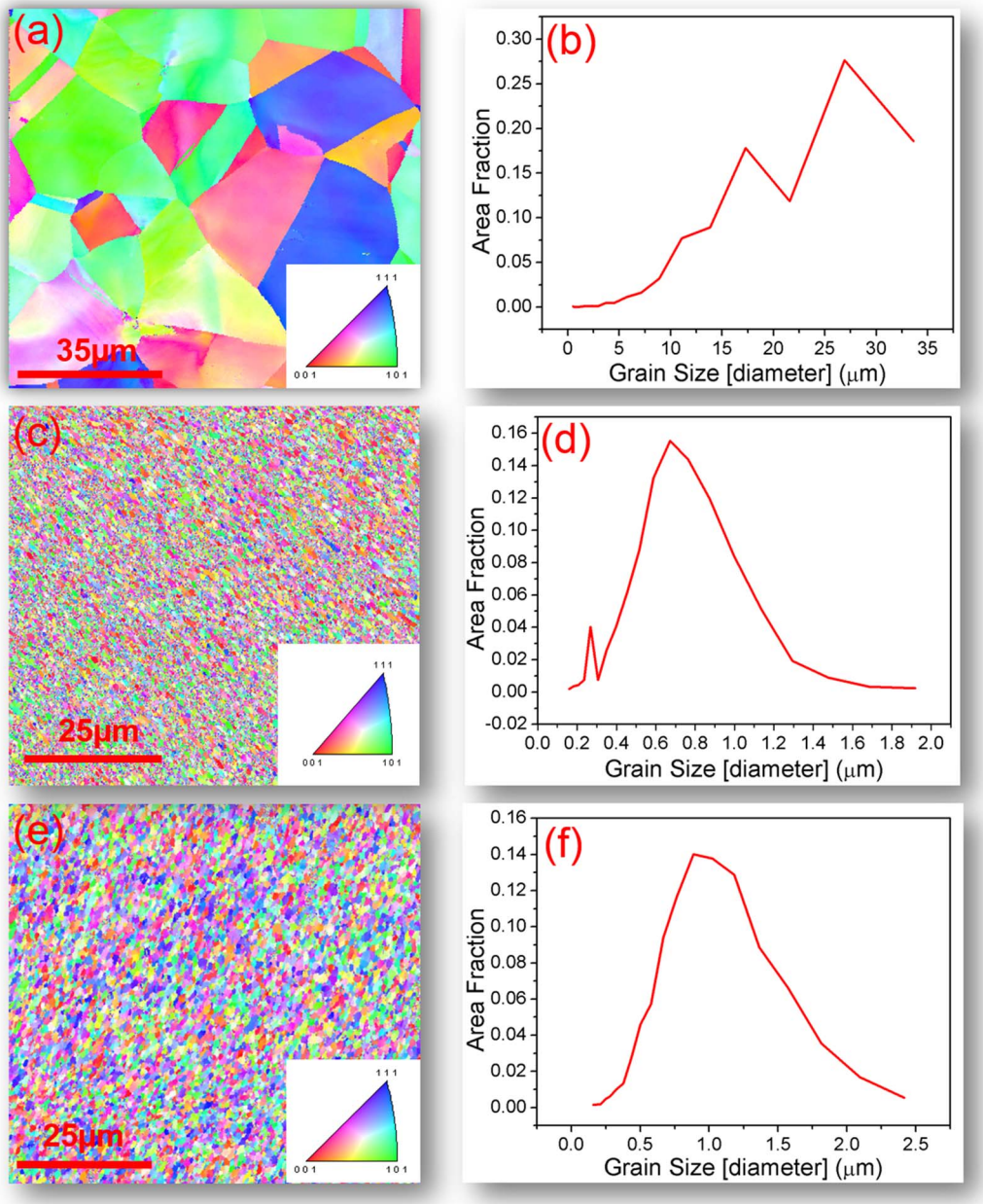

Fig. 3. (a) Electron back scatter diffraction (EBSD) image of as-received SS316L, (b) grain size distribution for as-received SS316L, (c) processed at 388 rpm (388-C), transverse speed of 20 mm/min and cooling at 0 °C, (d) grain size distribution for 388-C sample (e) processed at 1800 rpm (1800-C), transverse speed of 20 mm/min and cooling at 0 °C, (f) grain size distribution for 1800-C [34].

3.2. Cavitation erosion and corrosion

The results of pure cavitation erosion testing for all samples are shown in Fig. 6(a). All samples show incubation period during which material deforms plastically with negligible mass loss. The incubation period was nearly 2 h for the as-received alloy, 5 h for 388-C and 7 h for 1800-C specimens indicating significant increase in incubation period for the processed samples. In general, incubation period during cavitation erosion scales almost linearly with the yield strength [4] and recoverable indentation work (W_e) [39]. Both the processed samples have higher yield strength and larger recoverable indentation work (W_e) compared to as-received alloy which explains their higher incubation period. However, despite having higher yield strength and larger recoverable work, 388-C showed lower incubation period compared to 1800-C. This is likely due to significantly large martensite fraction present in 388-C (~45%) specimen compared to 1800-C (~8%) specimen. Martensite phase has higher hardness but lower ductility compared to austenitic phase resulting in brittle fracture during implosion of bubbles which likely decreased the incubation period. The incubation stage for all samples was followed by a steep rise in the mass loss which reaches a maximum and then ends into a steady-state regime (Fig. 6(a)). The cumulative volume loss (CVL) after 20 h of pure cavitation testing was 3 mm^3 for the as-received alloy, 0.75 mm^3 for 1800-C and 0.5 mm^3 for 388-C. Thus, 388-C showed nearly 6 times increase in the cavitation erosion resistance while it is nearly 4 times for 1800-C specimen. Higher strain-hardening rate and yield strength indicates higher resistance to plastic deformation while high elastic deformation signifies lower plastic energy absorbed by the specimen during deformation. Therefore, the observed significant increase in cavitation erosion resistance for processed specimens may be attributed

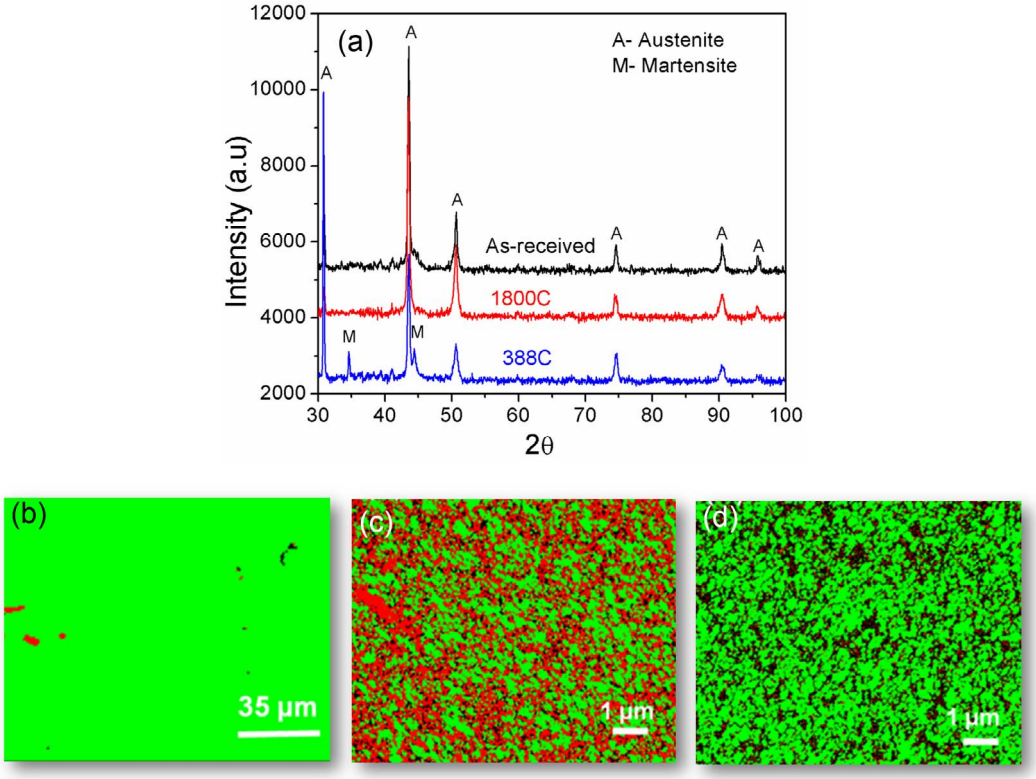

Fig. 4. (a) X-ray diffraction (XRD) analysis of as-received steel, 1800-C and 388-C specimens; EBSD Phase map for (b) as-received alloy (c) for the sample processed at 388 rpm (388-C), transverse speed of 20 mm/min and cooling at 0 °C, (d) for the sample processed at 1800 rpm (1800-C), transverse speed of 20 mm/min and cooling at 0 °C. Green color indicates austenite phase while red color indicates martensite. (For interpretation of the references to colour in this figure legend, the reader is referred to the web version of this article.)

to their higher yield strength (σ_y), larger elastic deformation (W_e) and higher strain-hardening rate (n).

Fig. 6(b) shows the cumulative volume loss (CVL) for all specimens in cavitation erosion-corrosion. The CVL curve for as-received alloy during erosion-corrosion is different than pure erosion. The as-received alloy show continuous increase in mass loss in erosion-corrosion while it showed an acceleration stage followed by deceleration in mass loss during pure erosion. There is no noticeable difference in curves for 388C and 1800-C. All specimen shows a drop-in incubation period compared to pure cavitation erosion. As-received alloy showed an incubation period of about 1 h, 1800-C specimen showed nearly 5 h while 388-C showed a gradual and continuous mass loss without showing any noticeable incubation period. Continuous increase in mass loss for the as-received alloy and decrease in incubation period during cavitation erosion-corrosion may be attributed to removal of the work-hardened layer due to corrosion. To further elaborate this behavior, standalone corrosion experiments were preformed (Section 3.3). In addition to decrease in incubation period, all specimen shows higher material loss during cavitation erosion-corrosion compared to pure cavitation erosion. The cumulative volume loss after 20 h of cavitation erosion-corrosion testing was nearly 4 mm^3 for the as-received alloy, about 1 mm^3 and 0.75 mm^3 for 1800-C and 388-C respectively. Thus, 1800-C and 388-C showed nearly 4 times and 5.3 times higher cavitation erosion-corrosion resistance relative to as-received alloy. Thus, both the

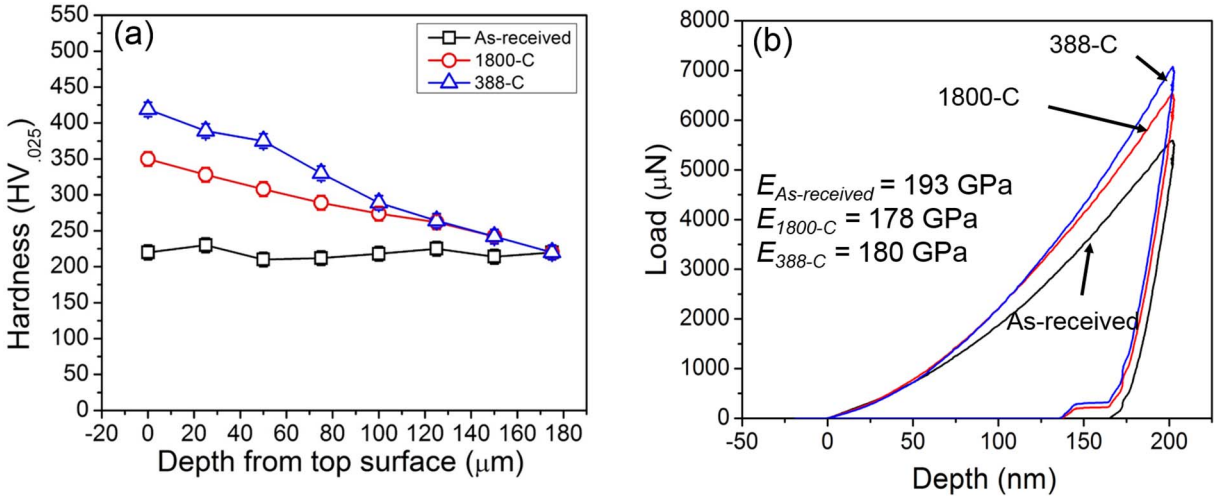

Fig. 5. (a) Vickers micro-hardness value for as-received steel, 388-C and 1800-C specimens; (b) elastic modulus for as-received steel, 388-C and 1800-C specimens.

Table 1
Strain hardening exponent index (n), yield strength from tabor expression, reversible work (W_e), irreversible work (W_i) and total indentation work (W_t) for all the samples.

Sample	Strain hardening exponent (n)	Yield strength (MPa)	Irreversible indentation work (W_i) × 10^5 (nJ)	Recoverable indentation work (W_e) × 10^5 (nJ)	Total indentation work (W_t) × 10^5 (nJ)
As-received	0.37	300	2.28	0.72	3.00
1800-C	0.43	425	2.55	1.05	3.60
388-C	0.47	443	2.57	1.18	3.75

processed specimen was able to retain similar superior performance in erosion-corrosion as in pure erosion. This is in contrast to cavitation erosion-corrosion behavior of $Al_{0.1}CrCoFeNi$ high entropy alloy (HEA) reported in our recent study [40]. HEA showed nearly 9 times higher resistance compared to stainless steel in pure erosion which drops to nearly 4 times in erosion-corrosion. HEA has significantly high corrosion resistance compared to stainless steel. The reduced degradation resistance for HEA under erosion-corrosion is attributed to removal of work-hardened layer. In the current study, the processed samples with higher yield strength were able to retain their performance in erosion-corrosion as well.

3.3. Potentiodynamic polarization

To understand the corrosion behavior, standalone electrochemical corrosion tests were done in 3.5% NaCl solution. The potentiodynamic polarization curves for all the specimens obtained from cyclic polarization are shown in Fig. 7(a)–(c). The corrosion current (I_{corr}) was obtained using Tafel fit from polarization curves and values are shown in Table 2. I_{corr} value is the lowest for 388-C, followed by 1800-C and largest for the as-received alloy, which is similar to the trend observed in order of grain size. This indicates direct correlation between corrosion rate and the grain size. Typically, SS316L forms passive layer which has a duplex structure with Fe_2O_3 (exhibiting n-type semiconductor characteristics) as an outer layer and Cr_2O_3 (exhibiting p-type semiconductor characteristics) as an inner layer. The donor to acceptor ratio in the passive layer has significant influence on the oxide layer characteristics. Typically, donor to acceptor concentration in passive layer decreases with grain size reduction [41], leading to decrease in charge carrier availability and better passivation. The donor to acceptor density further reduces in chloride environment, where chloride ion occupies oxygen vacancies in the passive film [36]. Thus, finer grain structure of processed samples contributed towards faster passivation kinetics, better passive layer stability, and superior corrosion resistance. In addition, the resistance to pit initiation, given by the factor $E_{pit} - E_{corr}$, where E_{pit} and E_{corr} are pitting potential and corrosion potential respectively, is higher for both the processed specimen (Table 2). This also corroborates higher stability of the passive film on the fine-grained structure. Enhanced pitting potential for processed samples is attributed to increase in Cr diffusion at the grain boundaries during grain refinement which promotes quicker passivation [22,42–44]. In addition, the adherence of passive layer to the surface is also enhanced with the grain refinement through oxide-pegging effect [44,45]. Higher pitting resistance for 1800-C compared to 388-C might be attributed to lower martensite fraction for the former (Fig. 4(c)). Martensite is known to have more negative galvanic potential compared to austenite [45] and it forms a micro-galvanic couple with the austenite phase promoting localized pitting.

3.4. Synergy

Probing the influence of erosion on corrosion and vice-versa, commonly referred as synergy, is important to fully understand the erosion-corrosion behavior. Synergy can be positive or negative for a particular material system and may vary with the test conditions [7]. Usually positive synergism exuberates material degradation while negative synergy reduces the material loss relative to their values in standalone test conditions. Synergy is composed of erosion component as erosion induced corrosion (EIC) and likewise, corrosion could promote erosion, referred as corrosion induced erosion (CIE). Synergy can be expressed by a relation given as : $V_T = V_E + V_C + V_{EIC} + V_{CIE}$ [46], where V_T is the total volume loss during cavitation erosion in 3.5% NaCl solution, V_E is volume loss during pure erosion, V_C is the volume loss calculated from corrosion current (i_{corr}) under static condition, V_{EIC} is the volume loss determined from the corrosion data for the sample subjected to pure erosion for 20 h, while V_{CIE} is the volume loss from corrosion induced erosion determined using the above empirical relation. Fig. 8(a) shows estimated volume loss from individual components, while Fig. 8(b) shows the percentage contribution of each factor to the total volume loss. It is evident that material loss is aggravated mostly through

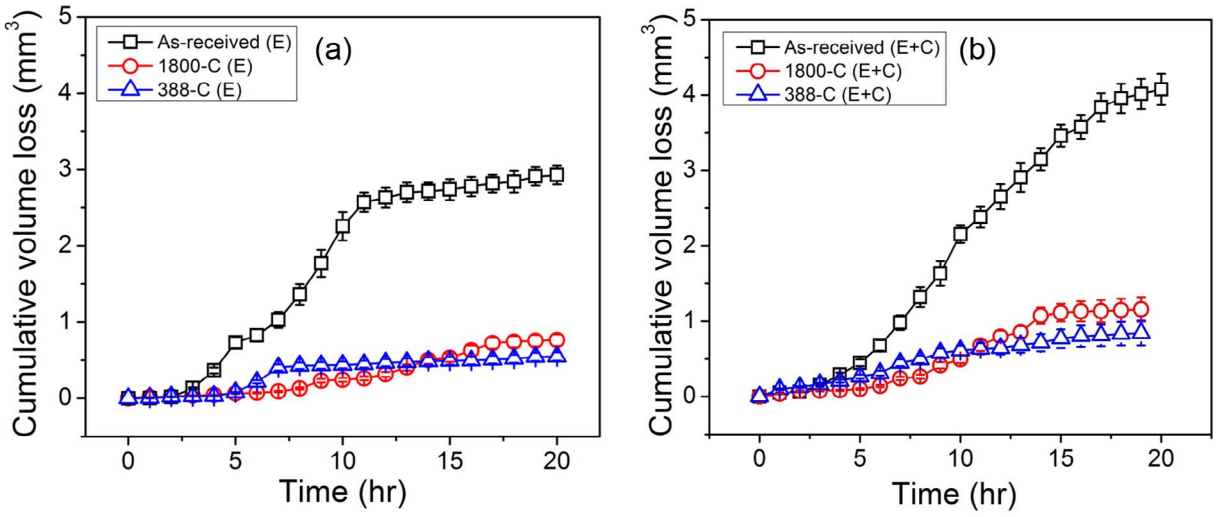

Fig. 6. (a) Cumulative volume loss for all samples subjected to pure cavitation erosion for 20 h (b) Cumulative volume loss for all samples subjected to cavitation erosion and corrosion under 3.5% NaCl for 20 h.

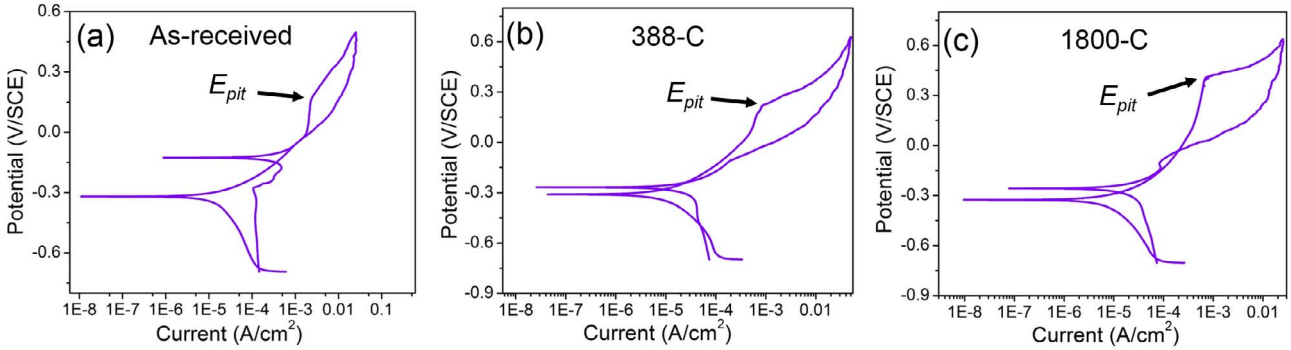

Fig. 7. (a) Cyclic Polarization (CP) curve for as-received steel, (b) CP curve for sample processed at 388 rpm (388-C), transverse speed of 20 mm/min and cooling at 0 °C, (c) CP curve for sample processed at 1800 rpm (1800-C), transverse speed of 20 mm/min and cooling at 0 °C.

Table 2
Corrosion current (I_{corr}), corrosion potential (E_{corr}), pitting potential (E_{pit}), $E_{pit} - E_{corr}$ and I_{corr} post erosion after 20 h.

Sample	I_{corr} (static) (μA)	E_{corr} (static) (mV)	E_{pit} (static) (mV)	$E_{pit} - E_{corr}$	I_{corr} (post 20 h erosion) (μA)
As-received	18	−294	359.8	653.8	3.5
388-C	6.54	−329	483.9	812.9	0.85
1800-C	13.40	−311	521	832	1.6

mechanical erosion and corrosion induced erosion. Distinctly, corrosion of eroded sample (EIC after 20 h) is significantly smaller compared to their corresponding static values, shown in Fig. 9(a). Some previous studies also report similar observation of lower corrosion rate of post-eroded samples, however, a rational explanation behind this anomaly is not provided in any of these studies. To probe the possible reason for the same, microstructure of 20 h eroded as-received specimen was obtained along the cross-section using optical microscope and is shown in Fig. 9(b). The grain size near the top edge of the sample was observed to be around 4–5 μm compared to 22 μm average grain size for the un-eroded as-received sample. This implies that cavitation resulted in appreciable grain refinement due to high strain-rate deformation. Both the processed samples have ultrafine grain structure which likely got further refined after the cavitation testing. The XRD data for all post-cavitation samples is shown in Fig. 9(c). All samples show considerable peak broadening which also support grain refinement of cavitation tested samples. The reduction in corrosion rate of cavitation tested samples might be attributed to strain-induced grain refinement during cavitation as indicated by faster passivation kinetics of finer grain structure discussed in Section 3.3. In addition to grain refinement, all samples show significant martensite formation (Fig. 9(c)) which likely occurred due to localized high strain-rate deformation during cavitation testing. Austenite to martensite transformation in stainless steel subjected to ultrasonic processing has been shown in earlier studies as well [47]{Rawers, 1991 #180}.

3.5. Damage mechanism

Fig. 10(a)–(d) shows SEM images of eroded samples. All samples exhibit similar damage mechanism including micro cracks, pits, craters and striations. As-received alloy shows deep craters while the processed samples show fine pits and cracks. Further, 1800-C and 388-C differ slightly in terms of their damage mechanisms. While 1800-C shows more striations and craters indicating plastic deformation, 388-C depict brittle behavior as evident by the presence of longer cracks (Fig. 10(c)). Striations are produced as a result of repetitive impacts of imploding bubbles resulting in fatigue loading, while slip bands formed under cyclic load during cavitation acts as nucleation site for micro-cracks. Inhibiting slip band formation and propagation can decrease the

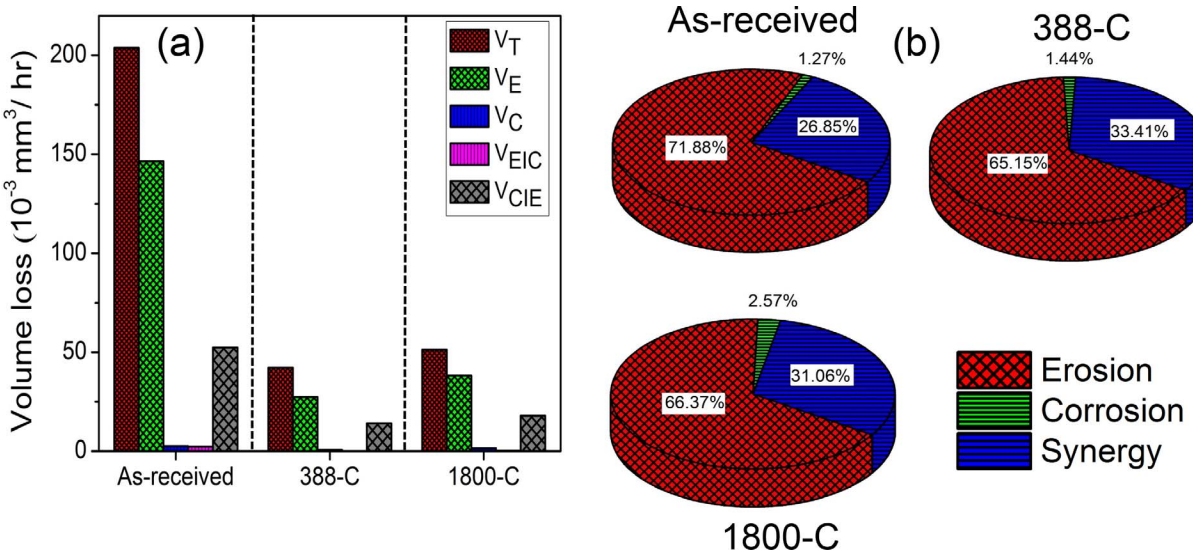

Fig. 8. (a) Total volume loss (V_T) in 3.5% NaCl, volume loss under pure erosion (V_E), volume loss from pure corrosion (V_C), volume loss from erosion induced corrosion (V_{EIC}) and volume loss from corrosion induced erosion (V_{CIE}) for as-received steel, sample processed at 388 rpm (388-C), transverse speed of 20 mm/min and cooling at 0 °C and sample processed at 1800 rpm (1800-C), transverse speed of 20 mm/min and cooling at 0 °C (b) percentage contribution of erosion , corrosion and synergy components in total volume loss for as-received, 388-C and 1800-C.

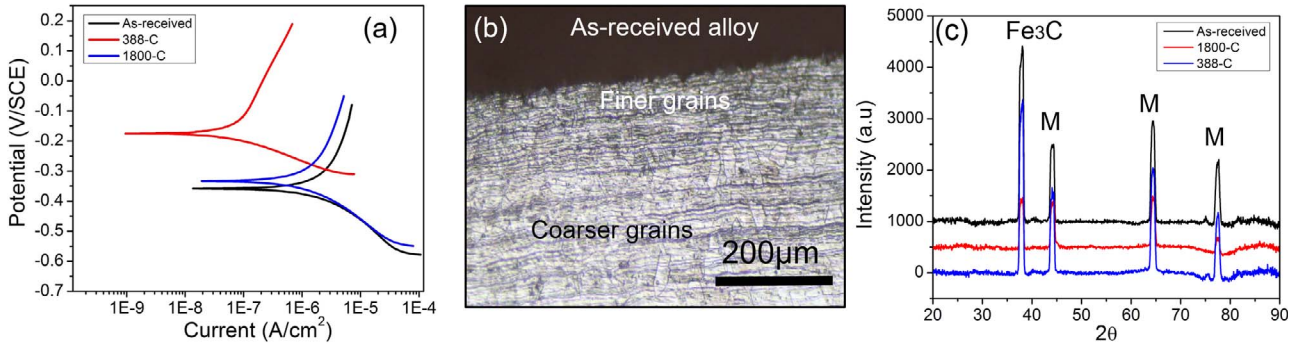

Fig. 9. (a) Tafel plot for as-received, 388-C and 1800-C samples after pure erosion test for 20 h; (b) Cross-section image of pure cavitation eroded as-received sample after 20 showing the grain size refinement in post-eroded samples; (c) XRD data for as-received, 388-C and 1800-C post cavitation for 20 h samples. All post cavitation samples show significant martensitic (*M*) formation.

nucleation sites for micro-cracks, thereby reducing the material failure by cavitation erosion. Grain boundaries are known to restrict the slip band growth [1], therefore, increase in grain boundary area is likely to enhance the cavitation erosion resistance. This correlates well with higher cavitation erosion resistance of 1800-C and 388-C. To get further insight into the superior cavitation erosion resistance of processed samples, the bubble diameter and micro-jet diameter during cavitation erosion was estimated using the approach as suggested by Plesset and Mitchell [48] and Ahmed et al [49]. The bubble diameter can be expressed as [48],

$$\left[\frac{dR}{dt}\right]^2 = \frac{2P}{3\rho}\left[1-\frac{R_0^3}{R^3}\right]-\frac{2\sigma}{\rho R}\left[1-\frac{R_0^2}{R^2}\right]$$

where R is radius of the bubble for time t, R_0 is initial radius of the bubble, P is fluid pressure, ρ is density of the fluid and σ is the surface

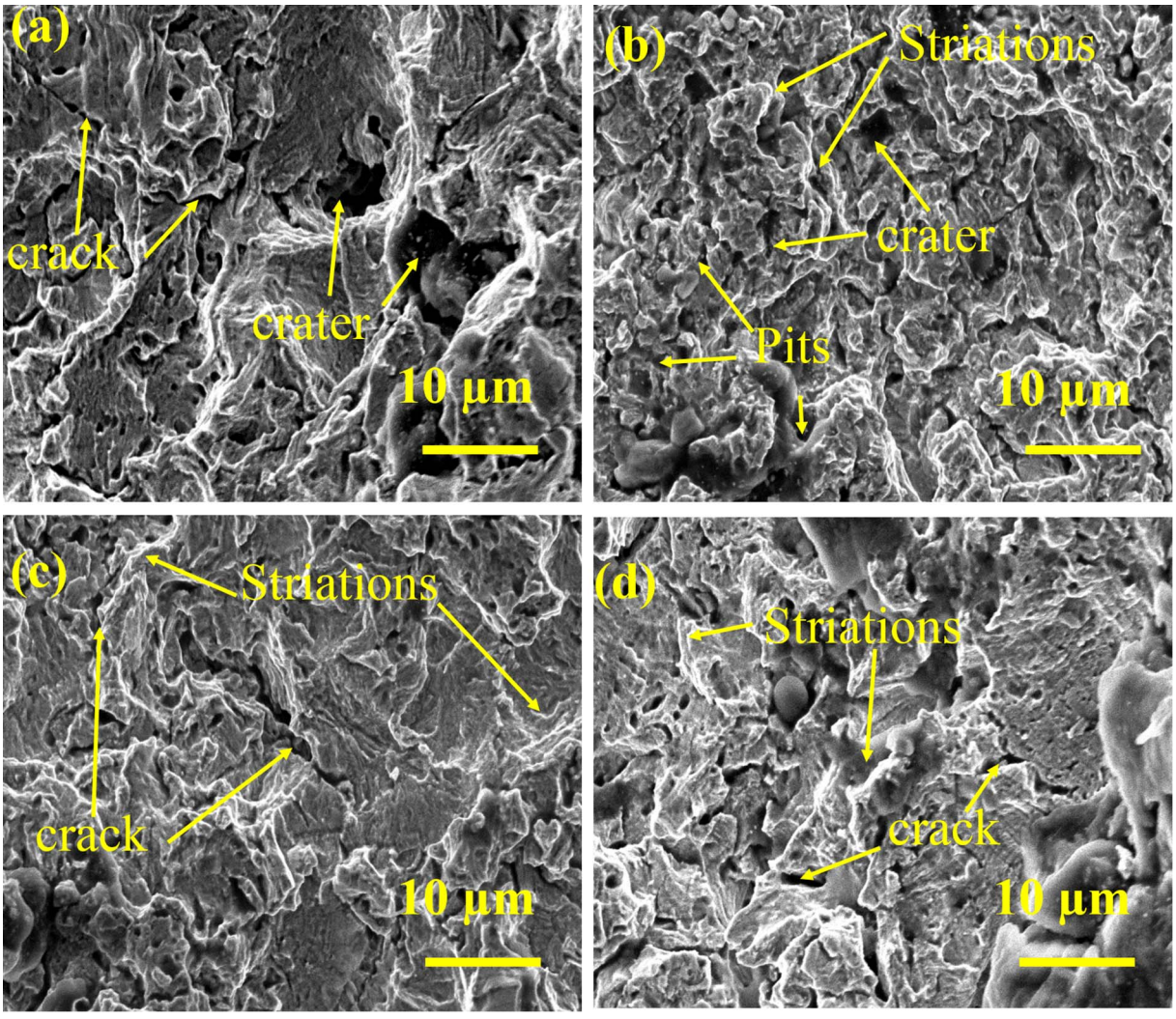

Fig. 10. (a) SEM image of as-received eroded sample, (b) sample processed at 1800 rpm (1800-C), transverse speed of 20 mm/min and cooling at 0 °C (c) sample processed at 388 rpm (388-C), transverse speed of 20 mm/min and cooling at 0 °C, (d) SEM image of as-received cavitation erosion-corrosion sample.

tension constant. The bubble diameter at 20 kHz frequency and 50 μm amplitude was estimated to be 1 mm. The diameter of micro-jet (d_j) can be estimated from the bubble diameter (d_o) using $d_j = d_0/20c$, where c is the amplitude of vibrator [29], which gives d_j nearly as 1–2 μm [49]. Thus, the size of micro-jets is of the order of average grain-size of 1800-C and 388-C specimens while it is significantly smaller compared to the average grain size for the as-received alloy. This suggests that bubble implosion is highly localized and most likely occurred within a single grain for the as-received alloy while it is more uniform phenomenon that occurred in multiple grains and grain boundaries for both the processed samples. Thus, both the processed samples are additionally benefitted by grain boundary strengthening which is uncertain for the as-received alloy due to its significantly bigger grain compared to bubble diameter. The results of current study suggest that fine grained materials achieved using submerged friction stir processing show remarkably high cavitation erosion and erosion-corrosion resistance making them promising materials for cavitating environment.

4. Conclusion

In the current investigation, submerged friction stir processing was utilized to develop tailored microstructures in stainless steel. High strain-rate processing at 1800 rpm resulted in nearly single-phase microstructure with average grain size of 0.9 μm while lower strain-rate processing at 388 resulted in a two-phase microstructure with average grain size of nearly 0.6 μm. Depending on the microstructure, the processed sample demonstrated 4–6 times higher cavitation erosion resistance. Both the processed sample were able to maintain their superior performance in erosion-corrosion environment as well. The remarkable improvement in erosion-corrosion behavior of processed samples was explained by surface strengthening, higher strain-hardening and larger recoverable indentation work. Processed samples also demonstrated higher corrosion resistance in standalone corrosion testing which was attributed to faster passivation kinetics of fine grained structure and higher pitting resistance. The post-eroded samples showed decrease in corrosion rates which signifies corrosion induced erosion to have larger contribution in material degradation rather than erosion induced corrosion.

References

[1] C. Heathcock, B. Protheroe, A. Ball, Cavitation erosion of stainless steels, Wear 81 (1982) 311–327.
[2] A. Karimi, J.L. Martin, Cavitation erosion of materials, Int. Met. Rev. 31 (1986) 1–26.
[3] Ramon Garcia, Frederick G. Hammitt, Cavitation Damage and Correlation with Material and Fluid Properties, 5031-II-I (1966).
[4] R. Richman, W. McNaughton, Correlation of cavitation erosion behavior with mechanical properties of metals, Wear 140 (1990) 63–82.
[5] K. Lo, F. Cheng, C. Kwok, H. Man, Improvement of cavitation erosion resistance of AISI 316 stainless steel by laser surface alloying using fine WC powder, Surf. Coat. Technol. 165 (2003) 258–267.
[6] C. Kwok, F. Cheng, H. Man, Synergistic effect of cavitation erosion and corrosion of various engineering alloys in 3.5% NaCl solution, Mater. Sci. Eng., A 290 (2000) 145–154.
[7] R.J. Wood, Erosion–corrosion interactions and their effect on marine and offshore materials, Wear 261 (2006) 1012–1023.
[8] R.E.A. Arndt, R.L. Voigt, J.P. Sinclair, P. Rodrique, A. Ferreira, Cavitation erosion in hydroturbines, J. Hydraul. Eng. 115 (1989) 1297–1315.
[9] W. Batten, A. Bahaj, A. Molland, J. Chaplin, Hydrodynamics of marine current turbines, Renewable Energy 31 (2006) 249–256.
[10] J.P. Tullis, Hydraulics of Pipelines: Pumps, Valves, Cavitation, Transients, John Wiley & Sons, 1989.
[11] H. Hiraga, T. Inoue, H. Shimura, A. Matsunawa, Cavitation erosion mechanism of NiTi coatings made by laser plasma hybrid spraying, Wear 231 (1999) 272–278.
[12] R. Singh, S.K. Tiwari, S.K. Mishra, Cavitation erosion in hydraulic turbine components and mitigation by coatings: current status and future needs, J. Mater. Eng. Perform. 21 (2012) 1539–1551.
[13] J.F. Santa, L.A. Espitia, J.A. Blanco, S.A. Romo, A. Toro, Slurry and cavitation erosion resistance of thermal spray coatings, Wear 267 (2009) 160–167.
[14] S. Momeni, W. Tillmann, M. Pohl, Composite cavitation resistant PVD coatings based on NiTi thin films, Mater. Des. 110 (2016) 830–838.
[15] A. Krella, A. Czyżniewski, Cavitation erosion resistance of Cr–N coating deposited on stainless steel, Wear 260 (2006) 1324–1332.
[16] T. Grögler, E. Zeiler, A. Hörner, S. Rosiwal, R. Singer, Microwave-plasma-CVD of diamond coatings onto titanium and titanium alloys, Surf. Coat. Technol. 98 (1998) 1079–1091.
[17] F. Cheng, S. Jiang, Cavitation erosion resistance of diamond-like carbon coating on stainless steel, Appl. Surf. Sci. 292 (2014) 16–26.
[18] R.S. Lima, B.R. Marple, Thermal spray coatings engineered from nanostructured ceramic agglomerated powders for structural thermal barrier and biomedical applications: a review, J. Therm. Spray Technol. 16 (2007) 40–63.
[19] H.L. de Villiers Lovelock, Powder/processing/structure relationships in WC-Co thermal spray coatings: a review of the published literature, J. Therm. Spray Technol. 7 (1998) 357–373.
[20] V.A.D. Souza, A. Neville, Aspects of microstructure on the synergy and overall material loss of thermal spray coatings in erosion–corrosion environments, Wear 263 (2007) 339–346.
[21] H.J.C. Voorwald, L.F.S. Vieira, M.O.H. Cioffi, Evaluation of WC-10Ni thermal spraying coating by HVOF on the fatigue and corrosion AISI 4340 steel, Procedia Eng. 2 (2010) 331–340.
[22] Z.J. Zheng, Y. Gao, Y. Gui, M. Zhu, Corrosion behaviour of nanocrystalline 304 stainless steel prepared by equal channel angular pressing, Corros. Sci. 54 (2012) 60–67.
[23] R. Valiev, Nanostructuring of metals by severe plastic deformation for advanced properties, Nat. Mater. 3 (2004) 511–516.
[24] R.S. Mishra, Z.Y. Ma, I. Charit, Friction stir processing: a novel technique for fabrication of surface composite, Mater. Sci. Eng., A 341 (2003) 307–310.
[25] J.-Q. Su, T.W. Nelson, C.J. Sterling, Friction stir processing of large-area bulk UFG aluminum alloys, Scr. Mater. 52 (2005) 135–140.
[26] C.J. Hsu, C.Y. Chang, P.W. Kao, N.J. Ho, C.P. Chang, Al–Al3Ti nanocomposites produced in situ by friction stir processing, Acta Mater. 54 (2006) 5241–5249.
[27] W. Wang, Q.-Y. Shi, P. Liu, H.-K. Li, T. Li, A novel way to produce bulk SiCp reinforced aluminum metal matrix composites by friction stir processing, J. Mater. Process. Technol. 209 (2009) 2099–2103.
[28] C.I. Chang, X.H. Du, J.C. Huang, Achieving ultrafine grain size in Mg–Al–Zn alloy by friction stir processing, Scr. Mater. 57 (2007) 209–212.
[29] M. Hajian, A. Abdollah-Zadeh, S. Rezaei-Nejad, H. Assadi, S. Hadavi, K. Chung, M. Shokouhimehr, Improvement in cavitation erosion resistance of AISI 316L stainless steel by friction stir processing, Appl. Surf. Sci. 308 (2014) 184–192.
[30] J. Escobar, E. Velásquez, T. Santos, A. Ramirez, D. López, Improvement of cavitation erosion resistance of a duplex stainless steel through friction stir processing (FSP), Wear 297 (2013) 998–1005.
[31] H.S. Grewal, H.S. Arora, H. Singh, A. Agrawal, Surface modification of hydroturbine steel using friction stir processing, Appl. Surf. Sci. 268 (2013) 547–555.
[32] K. Selvam, B. Rakesh, H. Grewal, H. Arora, H. Singh, High strain deformation of austenitic steel for enhancing erosion resistance, Wear 376 (2017) 1021–1029.
[33] A. Rollett, F. Humphreys, G.S. Rohrer, M. Hatherly, Recrystallization and Related Annealing Phenomena, Elsevier, 2004.
[34] K. Selvam, A. Ayyagari, H.S. Grewal, S. Mukherjee, H.S. Arora, Enhancing the erosion-corrosion resistance of steel through friction stir processing, Wear 386–387 (2017) 129–138.
[35] M. Isakov, S. Hiermaier, V.-T. Kuokkala, Effect of strain rate on the martensitic transformation during plastic deformation of an austenitic stainless steel, Metall. Mater. Trans. A 46 (2015) 2352–2355.
[36] H. Nakagawa, T. Miyazaki, Effect of retained austenite on the microstructure and mechanical properties of martensitic precipitation hardening stainless steel, J. Mater. Sci. 34 (1999) 3901–3908.
[37] A. Giannakopoulos, S. Suresh, Determination of elastoplastic properties by instrumented sharp indentation, Scr. Mater. 10 (1999) 1191–1198.
[38] G.R. Lehnhoff, K.O. Findley, The martensitic transformation and strain-hardening behavior of austenitic steels during fatigue and tensile loading, JOM 66 (2014) 756–764.
[39] J.F. dos Santos, C.M. Garzón, A.P. Tschiptschin, Improvement of the cavitation erosion resistance of an AISI 304L austenitic stainless steel by high temperature gas nitriding, Mater. Sci. Eng., A 382 (2004) 378–386.
[40] R. Nair, H. Arora, S. Mukherjee, S. Singh, H. Singh, H. Grewal, Exceptionally high cavitation erosion and corrosion resistance of a high entropy alloy, Ultrason. Sonochem. 41 (2018) 252–260.
[41] L. Jinlong, L. Hongyun, Effect of temperature and chloride ion concentration on corrosion of passive films on nano/ultrafine grained stainless steels, J. Mater. Eng. Perform. 23 (2014) 4223–4229.
[42] M. Pisarek, P. Keedzierzawski, M. Janik-Czachor, K. Kurzydlowski, Effect of hydrostatic extrusion on the corrosion resistance of type 316 stainless steel, Corrosion 64 (2008) 131–137.
[43] M. Rifai, H. Miyamoto, H. Fujiwara, Effects of strain energy and grain size on corrosion resistance of ultrafine grained Fe-20% Cr steels with extremely low C and N fabricated by ECAP, Int. J. Corros. 2015 (2015).
[44] J. Tien, F. Pettit, Mechanism of oxide adherence on Fe-25Cr-4Al (Y or Sc) alloys, Metall. Trans. 3 (1972) 1587–1599.
[45] A. Hamada, L. Karjalainen, M. Somani, Electrochemical corrosion behaviour of a novel submicron-grained austenitic stainless steel in an acidic NaCl solution, Mater. Sci. Eng., A 431 (2006) 211–217.
[46] R. Wood, S. Hutton, The synergistic effect of erosion and corrosion: trends in published results, Wear 140 (1990) 387–394.
[47] J.C. Rawers, R.A. McCune, J.S. Dunning, Ultrasound treatment of centrifugally atomized 316 stainless steel powders, Metall. Trans. A 22 (1991) 3025–3033.
[48] M. Plesset, T. Mitchell, On the stability of the spherical shape of a vapor cavity in a liquid, Q. Appl. Math. 13 (1956) 419–430.
[49] S. Ahmed, K. Hokkirigawa, R. Oba, Fatigue failure of SUS 304 caused by vibratory cavitation erosion, Wear 177 (1994) 129–137.